Structural, optical, and electronic properties of single crystals of 4H lead-based hexagonal hybrid perovskite

Florent Pawula, Ali Fakih, Stanislav Péchev, Ramzy Daou, Daniele Mantione, Oleg Lebedev, Antoine Maignan, Georges Hadziioannou, Sylvie Hébert, Guillaume Fleury

Structural, optical and electronic properties of single crystals of 4H lead-based hexagonal hybrid perovskite

Florent Pawula[1, *], Ali Fakih[2], Stanislav Pechev[3], Ramzy Daou[2], Daniele Mantione[1], Oleg Lebedev[2], Antoine Maignan[2], Georges Hadziioannou[1], Sylvie Hébert[2, *] and Guillaume Fleury[1]

[1] Univ. Bordeaux, CNRS, Bordeaux INP, LCPO, UMR 5629, F-33600 Pessac, France
[2] Normandie Univ, ENSICAEN, UNICAEN, CNRS, CRISMAT, 14000 Caen, France
[3]Univ. Bordeaux, CNRS, Bordeaux INP, ICMCB, UMR 5026, F-33600 Pessac, France

* Corresponding author: florent.pawula@cnrs-imn.fr, sylvie.hebert@ensicaen.fr

Abstract

Lead halide hybrid perovskite single crystals have been grown using antisolvent vapor-assisted crystallization. The chemical composition and structural model of the crystals have been established using nuclear magnetic resonance and single crystal X-ray diffraction, leading to the formula $FA_{0.9}MA_{0.1}PbI_{2.23}Br_{0.77}$. The hexagonal crystallographic structure with *P6₃/mmc* space group has been confirmed by transmission electron microscope study. Through a detailed analysis of the single crystal XRD data, the locations of FA^+ and MA^+ in the unit cell have been identified, and the off-centering of Pb^{2+} on the octahedral sites has been unveiled, probably due to the Pauli repulsion of the lone-pair. This material is a wide-gap semiconductor with Eg = 2.27 eV and demonstrates photoluminescence activity. The thermal conductivity is disorder-dominated with an extremely low value of 0.17 $W.m^{-1}.K^{-1}$ from about 75 K up to 325 K. The present investigation on $FA_{0.9}MA_{0.1}PbI_{2.23}Br_{0.77}$ single crystal demonstrates that low values of thermal conductivities are obtained in this hexagonal family of hybrid halide perovskites, with mixed cationic and anionic disorder.

Introduction

For many years the hybrid halide perovskites have received great attention by the scientific community due to their very promising potential for technological applications. The hybrid perovskites ABX_3 family gathers the compounds where A is an organic cation, B is an inorganic cation and X is a halide. The most studied members are those constituted of $A = MA^+, FA^+$; $B = Pb^{2+}, Sn^{2+}$; and $X = I^-, Br^-, Cl^-$, where MA^+ and FA^+ stand for methylammonium $CH_3NH_3^+$ and formamidinium $NH_2CHNH_2^+$, respectively. This family includes materials with a range of interesting properties such as optoelectronic, semiconductivity, low thermal conductivity, or large Seebeck coefficients, which hold great promise for many applications, including photovoltaics, thermoelectricity and thermal insulation [1–3]. Engineering the density of electronic states and lattice dynamics to fine-tune the functional properties can be achieved through a careful balance of the chemical composition. For example, several publications report on photovoltaic cell efficiency above 20% by controlling the composition to tune the band gap, charge carrier transport and charge recombination [4–6].

The hybrid perovskites have different crystallographic structures, e.g. cubic as in the widely investigated $(MA)PbI_3$ or $(MA)PbBr_3$, or 2H, 4H, 6H or 9R hexagonal as in $(DMA)PbX_3$ ($X = Cl^-$ or Br^-) or $(Az)PbX_3$ ($X = I^-, Cl^-$ or Br^-) [7–9] depending on the nature of the A cation or the nature of the X site [10]. Remarkably, the thermal conductivity is very low, 0.34 and 0.73 $W.m^{-1}.K^{-1}$ at 300K for $MAPbX_3$ ($X = I^-, Cl^-$) [11,12] and the photovoltaic performance is promising with a conversion efficiency reaching 20% in $(FA_{0.85}MA_{0.15})_{0.95}PbI_{2.55}Br_{0.45}$ [5,13], these properties being reported only for thin films. Few reports of the physical properties of hybrid lead halide hexagonal perovskite single crystals with mixed cations and anions have been published. Interestingly, studying hexagonal perovskites and their derivatives offer greater structural diversity than cubic perovskites, leading to unique arrangements of *M*-*X* octahedra, shorter *M*-*M* distances along with narrower *M*-*X*-*M* bond angles, which, in turn, have a profound

impact on their properties, e.g. magnetism. These materials, particularly those based on dimers, have been the focus of extensive research in materials physics. For example, hexagonal transition metal oxide perovskites are currently of significant interest for their potential to introduce geometrical frustration in magnetic ordering at low temperatures, making them important in the field of quantum materials [14]. The analogy between hexagonal transition metal oxide perovskites and hexagonal halide perovskites is relevant to illustrate the possibilities brought by hexagonal crystallographic structure.

We report here on the single crystal growth of this Pb-based hybrid perovskite and on the determination of the physical properties of these single crystals. Targeting the composition of that material reported to be efficient for solar cell conversion [5,13], $FA_{0.85}MA_{0.15}PbI_{2.55}Br_{0.45}$ single crystals have been prepared by antisolvent vapor-assisted crystallization (AVC). The refined structure and chemical composition were determined using single-crystal X-ray diffraction (SC-XRD) and quantitative nuclear magnetic resonance (NMR). Here we report the detailed crystallographic structure of this lead halide hexagonal hybrid perovskite single crystal, empirically $FA_{0.9}MA_{0.1}PbI_{2.23}Br_{0.77}$, along with the investigation of its microstructure, optical and T-dependent dielectric properties and thermal conductivity.

Experimental

The starting materials methylammonium bromide (MABr), formamidinium iodide (FAI), lead(II) bromide ($PbBr_2$), dimethylsulfoxide (DMSO), N,N-dimethylformamide (DMF) and dichloromethane (DCM) were bought from Sigma Aldrich; lead(II) iodide (PbI_2) was bought from TCI. Crystals of nominal $FA_{0.85}MA_{0.15}PbI_{2.55}Br_{0.45}$ composition were synthesized by Antisolvent Vapor-assisted Crystallization (AVC) at room temperature [15]. A solution of 1:4 DMSO:DMF containing stoichiometric amounts of MABr:$PbBr_2$:FAI with excess PbI_2 was solubilized by manual shaking before being introduced in the inner vial. The vial was placed in

a jar containing DCM as antisolvent. After a few days, macroscopic crystals appeared and were left grown until suitable size for characterizations, i.e. about a few millimeters. The samples were then dried under vacuum overnight at 65°C.

Single-crystal X-ray diffraction experiment was carried out at 299 K. Diffraction data collection was performed using a Bruker Kappa Apex II single-crystal diffractometer with Mo Kα radiation, equipped with an Oxford Cryosystems nitrogen Cryostream 700 plus. Olex2 GUI [16] was used for structure resolution and refinement. The structure was solved with the SHELXT [17] software using Intrinsic Phasing method and refined with SHELXL [18] and a Least Squares minimization.

Transmission electron microscopy (TEM) including electron diffraction (ED) and high-resolution TEM (HRTEM) experiments was performed using an aberration image and probe-corrected JEM ARM200F cold FEG microscope operated at 80-200kV equipped with a CENTURIO EDX detector, Orius Gatan CCD camera and GIF Quantum spectrometer. TEM sample was prepared by crushing the sample in an agate mortar with ethanol followed by the deposition of the obtained suspension on Cu carbon holey grid.

The ^{1}H and ^{13}C Nuclear Magnetic Resonance (NMR) spectra of few solubilized crystals were recorded at room temperature in deuterated DMSO D6 (99.8% D, H_2O < 0.02%, Eurisotop) using a 400 MHz Bruker Advance 300 spectrometer. Heteronuclear Single Quantum Correlation (HSQC) and Quantitative NMR analyses were carried out by the addition of diiodomethane (> 99%, Acros Organics) in 1:1 molar ratio in the NMR tube. The ^{13}C quantitative NMR has been recorded with an Inverse Gate (IG) scan with two different relaxation times, 2 seconds, and 30 seconds without any difference in the integrals.

Crushed-crystal powder was sifted on a small amount of grease on a glass substrate to measure the UV-vis and photoluminescent (PL) properties. The UV-vis spectra were recorded

on a SHIMADZU UV-2600 UV/Vis spectrophotometer equipped with an integrated sphere and the PL spectra were recorded on a HORIBA FluoroMax-4 Spectrofluorometer.

Temperature-dependent dielectric measurements with a 1 V AC bias were carried out using an LCR meter (Agilent 4284A) with a homemade sample probe integrated into the Physical Properties Measurement System (PPMS, Quantum Design). A single crystal was polished to form two parallel faces of a capacitor of dimensions $S = 0.99 \times 1.61$ mm^2 and a thickness d = 0.30 mm. Isopropanol-based carbon paste was painted on each face to prepare the electrodes.

Thermal conductivity was measured on a $0.5 \times 0.7 \times 1.9$ mm^3 crystal in a custom-built sample holder installed in a PPMS cryostat using a steady-state technique including a calibrated heat pipe to account for thermal losses (principally due to radiation) at relatively high temperatures by measuring the input power to the sample [19]. This radiative loss was negligible below 150 K. Additional calculated radiation losses were less than 10% of the measured power at 300 K.

Results and Discussion

Structural analyses

After crystallization by AVC, hexagonal orange crystalline objects from a few hundred μm^3 up to about a few mm^3 were harvested and single-crystal X-ray diffraction data were collected. The refined crystal structure at 299 K is consistent with a hexagonal unit cell and the centrosymmetric *P6₃/mmc* space group. Details of the structure refinements and a photograph of the crystals are available in supplementary material – Table S1 and Figure S1 respectively. The Goldschmidt tolerance factor for the retained formula is $t = 0.98 \pm 0.06$, indicative of a cubic structure hypothesizing spherical ionic radii and considering r(MA^+) = 217 pm, r(FA^+) = 253 pm, r(Pb^{2+}(VI)) = 119 pm, r(I^-(VI)) = 220 pm, and r(Br^-(VI)) = 196 pm [20]. However, the margin of error, about 6%, suggests the possibility of hexagonal or tetragonal structures ($t > 1$).

Nevertheless, the phase stability of Pb hybrid perovskites with mixed FA^+/MA^+ and mixed Br^-/I^- compositions, including multiple configuration of the molecules' orientation in first-principles calculations has been recently reported [10]. The predictions for the same chemical composition as presented here indicate that the most stable structure is hexagonal.

As displayed in **Figure 1 a)**, the material crystallizes in ABX_3 4H perovskite structure with the following lattice parameters at 299 K: a = 8.7964(6) Å, c = 15.1514(12) Å, c/a = 1.7225, V = 1015.3(2) $Å^3$ and Z = 4. The elementary lattice is constituted of two corner-sharing Pb_2X_9 (X = Br, I) dimers composed of two face-sharing PbX_6 octahedra. Accordingly, Pb^{2+} (4*f*) is in coordination VI on a distorted octahedral site; Br^- and I^- share statistically two sites – 6*g* and 6*h*. As shown in **Figure 1** and in **Table 1**, the 6*h* site, forming the belt of the dimer, mainly contains I^- at 87(1) % while the 6*g* site contains 60(2) % I^- and 40(2) % Br^-. Regarding the organic cations, their presence and amount have been determined by ^1H, ^{13}C NMR, and HSQC data analysis (see Figure S2).

Locating the light MA^+ and FA^+ groups and refining the C and N atoms' positions within a framework of elements, such as Pb, Br, and I, is difficult as the Fourier transform electron density maps are largely dominated by the heavy elements. Moreover, in the present work, we observed a strong collapse of the intensities of the X-ray diffraction peaks below 0.75 Å, rather than the usual gradual scattering weakening at high resolution observed in inorganic crystals. This could be related to some disorder of the organic groups [21]. However, the structure refinement of the Pb-X perovskite framework revealed a residual electronic density of around 3.0 $e.Å^{-3}$ in the unit cell, close to the *2a* and *2c* sites at *0, 0, 0,* and *1/3, 2/3, 1/4* respectively, where the organic cations are expected to be. The isoelectronic residual density volumes are displayed in **Figure 1**, where it can be noticed that the *2c* and *2a* site-centered voids are elongated along the *c* axis. The BYPASS method [22] was used to improve refinement by including the amount of organic cations. This method is originally designed to model disordered

solvent molecules within a structure on the basis of the observed electron density and the available void volumes. An amount of 84 electrons was found in the total voids' volume available over the unit cell. This is consistent with a composition close to $(FA_{0.4}MA_{0.6})PbI_{2.23}Br_{0.77}$. This cationic composition should be taken with caution since FA^+ and MA^+ are statistically distributed over the two voids at the *2a* and *2c* sites and the BYPASS method cannot refine FA versus MA ratio in each sites. Nonetheless, the BYPASS method is relevant to improve the global refinement and led to a consistent improvement of the quality fit criteria from R1 = 5.17 %, wR2 = 17.06 % to R1 = 2.93 %, and wR2 = 7.86 % at 299 K. It is worth mentioning that no improvement has been observed including solvent molecules (such as DMSO molecules used for crystal growth) in the BYPASS method. In order to better investigate the organic cations amount, quantitative ^{13}C NMR was performed, leading to FA^+ = 0.89 and MA^+ = 0.12. Hence, we retained the final chemical composition $FA_{0.9}MA_{0.1}PbI_{2.23}Br_{0.77}$, which is relatively close to the nominal chemical composition $FA_{0.85}MA_{0.15}PbI_{2.55}Br_{0.45}$. Nevertheless, the disparity in halide content may be attributed to various growth mechanisms, including for example, solvent's nature, local ionic diffusion rates or condensation kinetics, which could have favored the incorporation of bromine over iodine. These mechanisms are influenced by the solvent coordination ability and the different solvents coordination with lead and lead halide anions could be at the origin of the disparity [23].

Details of the fine structure are depicted in **Figure 2**. The bond lengths of Pb-*X*(6*h*) are about 2.4 % longer than the Pb-*X*(6*g*) ones at 299 K. Hence, the Pb^{2+} cations are off-centered along the *c* axis toward the extremities of the Pb_2X_9 dimers as illustrated by the large grey arrows in **Figure 2 a)**. Noteworthy, contrary to $DMAPbX_3$ (*X* = Br, Cl) [8] there is no off centering in the *ab* plane as observed in **Figure 2 b**). Distortion of dimers in hybrid perovskite has been the subject of a recent report in which it was demonstrated that the distortion is induced by the lone pair of Pb, displacing the cation in the opposite direction of the lone pair [24]. Therefore, the

lone pairs in Pb_2X_9 dimers should be pointing to one another.

Analyzing the structural parameters, an intriguing peculiarity is the displacement parameters on the anionic sites. The Br^-/I^- thermal displacement parameters are very anisotropic while the ones of Pb cations on *4f* site are only slightly anisotropic, as shown by the ellipsoids in **Figure 2**. The equivalent isotropic displacement value U_{eq} is 1.6 times higher in the 6*g* site than in the 6*h* site at 299 K (see **Table 1**). This should be induced by the 3D $[PbI_3]^-$ network which has a primary role in the lattice dynamics of hybrid lead halide perovskites with respect to the organic cations [25]. We hypothesized that this could arise from the Pauli repulsion of the two Pb lone pairs pointing to each other, displacing Pb atoms towards the extremities of the Pb_2X_9 dimers, and so inducing motions of the halides as shown for some halide perovskites [25].

The X-ray diffraction study is consistent with the room temperature transmission electron microscopy (TEM) observations, particularly with the bright field high-resolution TEM (BF HRTEM) and the electronic diffraction (ED) presented in **Figure 3**. The crushed crystals exhibit hexagonal nanoparticle-like thin platelets morphology (**Figure 3a**), with a typical thickness of about 25 nm thick as can be seen in the [100] direction (**Figure 3b**) and lateral size varying in the range of 200 - 400 nm. In addition, we note the presence of moiré patterns (**Figure 3d**) related to a disorder-induced phenomenon along the *c*-axis.

Optical properties

The room temperature absorption spectrum is displayed in **Figure 4**. This compound shows a transition related to the energy gap between the conduction band and the valence band in the visible spectral range at 535 nm, consistent with the yellowish color of the powder. Hypothesizing no or negligible absorbance of a sub-band gap energy, the Tauc method (see Figure S3) suggests the bandgap energy value is 2.27 eV considering direct allowed transition respectively. This classifies this material as a wide-gap semiconductor compared to 1.2 - 1.7

eV medium-gap semiconductors (Cs,FA,MA)(Sn,Pb)I_3 [26]. Like these semiconductors, the absorption edge is rather sharp despite the presence of blunt features on the absorption edge around 550 nm. Such behavior in the absorption edge could be induced by excitonic features or possibly to slight divergence of cations' or anions' ratios from crystal to crystal. This material is photoluminescent as demonstrated by the emission peak ~ 625 nm (1.98 eV), which is relatively close to Eg, consistent with the direct band gap hypothesis, and reaches a maximum emission intensity when excited at 530 – 550 nm. In the (FA,MA)(Sn,Pb)I_3 compounds, it has been shown that PL property is strongly related to defects [26,27] and structural disorder induced by ion heterogeneity could also play a role in these hexagonal perovskites. Still, the distinct electronic band structure resulting from the hexagonal crystallographic structure should play a major role on the difference in PL characteristics with those compounds.

Dielectric properties

Figure 5 shows the real part ϵ_r' of the relative dielectric constant ($\epsilon_r = \epsilon/\epsilon_0$, where ϵ_o is the permittivity of vacuum) from room temperature down to 10 K, plotted as a function of frequency for a given T (**Figure 5a**) or as a function of T for a given frequency (**Figure 5b**). At all temperatures, the value of ϵ'_r slightly decreases from 500 Hz to 10^5 Hz and then more strongly decreases above 10^5 Hz (**Figure 5a**). There is almost no temperature dependence from 125K to 300K, while ϵ'_r slightly decreases below 125K (**Figure 5b**), with a small maximum of ϵ'_r at a temperature ranging from 125K to 150K as shown in the inset of **Figure 5b**. An additional feature appears in the lower frequency range (between 500 Hz and 1 kHz) which is characterized by a small hump at around 240 K and an increase in ϵ'_r above 290 K. This could be due to a small amount of water which is adsorbed on the surface and grain boundaries or trapped in the sample [28]. These extrinsic contributions can be suppressed by increasing the frequency [28–31].

The inset of **Figure 5 a)** shows the T-dependent relative dielectric loss ϵ''_r. At low

temperatures (< 250 K) and all frequencies, the ϵ_r'' values are relatively large, ranging from few tenth to 2. Up to 300 K, the dielectric loss increases significantly only at low f ≤ 1 kHz, close to 12. Large values of ϵ_r'' have been previously reported in hybrid perovskite, as in $MAPbI_3$ [32] with values spanning from 10 to 100 at high T.

The T-dependent dielectric constant was measured in different $APbX_3$ hybrid perovskite materials with $A = MA^+$, FA^+ or DMA^+, and $X = Br^-$, I^- or Cl^-. As can be seen in **Table 2**, room temperature ϵ_r's were found to be equal to or less than 60 from 1 kHz up to 1 MHz. From this table, two trends can be suggested: (i) Considering MA^+ and substituting the halide from I^- to Br^- to Cl^-, the dielectric constant decreases in all the frequency range. A similar trend might be suggested for FA^+ but that should be considered carefully regarding the amount of available data. (ii) Considering I^- (or Br^-) and substituting MA^+ for FA^+, the dielectric constant decreases at 1 MHz. Here, the ϵ_r'(300 K) value of $FA_{0.9}MA_{0.1}PbI_{2.23}Br_{0.77}$ is about 18 for a frequency range of 0.5 - 100 kHz. This is a little higher than the one in $DMAPbCl_3$ with ϵ_r' (300 K) ~ 11 (16 - 100 kHz) [8] which has a very similar crystallographic structure to the sample in the present work. This suggests that the small value of ϵ_r'(300 K) is mainly due to the hexagonal crystallographic structure of this hybrid perovskite, with the organic cation and halide nature playing a secondary role.

Thermal conductivity

The thermal conductivity is very low and almost constant between 100 and 300 K as can be seen **Figure 6**. The small feature seen at 200 K is most likely an artifact of the measurement. The shape of the thermal conductivity over the entire temperature range is consistent with the presence of strong disorder. In the limit that the sample can be modelled as a collection of harmonic oscillators which exchange energy incoherently between nearest neighbours, an estimate of the lower bound on the thermal conductivity can be obtained from the sound

velocities [33]. These values are not available for our material but have been measured for the perovskites $FAPbI_3$ and $FAPbBr_3$ [34]. The minimum thermal conductivities for these less complex structures are shown as solid red and blue lines respectively. The similar shape of these calculated curves to the data supports the conclusion that we are in the limit of strong disorder, with 2 types of halides with mixed occupancies, and 2 organic cations sites. In the case of $FAPbBr_3$, it is the higher average sound velocity than that of $FAPbI_3$ that leads to a greater minimum thermal conductivity. Similar curves can be generated for $MAPbI_3$ and $MAPbBr_3$ and are both above the $FAPbI_3$ one (see Figure S4). Intuitively we understand that heavier cations lead to greater damping of the sound velocity, and the impact of this is reflected by the minimum thermal conductivity curves (FA is heavier than MA, I is heavier than Br). The increase in internal degrees of freedom of FA^+ may also cause scattering to increase, further dampening the thermal conduction. Both curves are higher than the current measured values, suggesting that the 4H hexagonal perovskite structure should display a similar or lower average sound velocity than $FAPbI_3$, all other things being equal.

Concluding remarks

A lead-based hybrid halide perovskite has been synthesized as a single crystal. The chemical composition of $FA_{0.9}MA_{0.1}PbI_{2.23}Br_{0.77}$ has been established through quantitative NMR and single-crystal XRD analysis. Analysis of the crystallographic structure leads to a hexagonal symmetry with the centrosymmetric $P6_3/mmc$ space group. FA^+ and MA^+ are aligned along the *c* axis in the 2*a* and 2*c* sites. Pb^{2+} is off-centered probably due to the steric effect of the Pb lone pairs pointing to one another in the Pb_2X_9 dimers. The material is a wide band gap semiconductor with Eg = 2.27 eV, considering direct allowed transition respectively, and is photoluminescent. The emission peak is at about 625 nm and reaches maximum intensity when excited at about 540 nm. The compound possesses a small relative dielectric constant ϵ_r' due

to the antiparallel configuration of Pb_2X_9 dimers, which causes the net polarization to decrease. Additionally, the dielectric loss is relatively high. The T-dependent thermal conductivity curve shows the presence of strong disorder with extremely low values, about 0.17 $W.m^{-1}.K^{-1}$ from 75 K to 325 K, smaller than all the calculated minimum thermal conductivity in the strong disorder limit of $FAPbI_3$, $FAPbBr_3$, $MAPbI_3$, and $MAPbBr_3$. Very small values of thermal conductivity are reported in different hybrid perovskites [34–37], this study shows that extremely small values are also obtained in these hexagonal hybrid perovskites. The doping of this material could be investigated to control the reduction of the band gap value or the increase of electrical conductivity for photovoltaic or thermoelectric applications.

Acknowledgments

The authors thank Dr. S. Mariotti for useful discussion and F. Veillon for the assistance with dielectric measurements. The authors acknowledge financial support from the LabEx AMADEUS ANR-10-LABEX-0042-AMADEUS and the LabEx EMC3 for financial support. This work was performed within the framework of the Equipex ELORPrintTec ANR-10-EQPX-28-01 and the Labex AMADEUS ANR-10-LABEX-0042-AMADEUS with the help of the French state Initiative d'Excellence IdEx ANR-10-IDEX-003-02.

References

[1] Y. Chen and E. Orgiu, ChemNanoMat **5**, 290 (2019).
[2] L. Mao, C. C. Stoumpos, and M. G. Kanatzidis, J. Am. Chem. Soc. **141**, 1171 (2019).
[3] H. Xie, S. Hao, J. Bao, T. J. Slade, G. J. Snyder, C. Wolverton, and M. G. Kanatzidis, J. Am. Chem. Soc. **142**, 9553 (2020).
[4] J.-Y. Seo, H.-S. Kim, S. Akin, M. Stojanovic, E. Simon, M. Fleischer, A. Hagfeldt, S. M. Zakeeruddin, and M. Grätzel, Energy Environ. Sci. **11**, 2985 (2018).
[5] C. Geffroy, E. Grana, T. Bessho, S. Almosni, Z. Tang, A. Sharma, T. Kinoshita, F. Awai, E. Cloutet, T. Toupance, H. Segawa, and G. Hadziioannou, ACS Appl. Energy Mater. **3**, 1393 (2020).
[6] M. A. Green, E. D. Dunlop, J. Hohl-Ebinger, M. Yoshita, N. Kopidakis, and A. W. Y. Ho-Baillie, Prog. Photovolt. Res. Appl. **28**, 3 (2020).
[7] P. Gratia, I. Zimmermann, P. Schouwink, J.-H. Yum, J.-N. Audinot, K. Sivula, T.

Wirtz, and M. K. Nazeeruddin, ACS Energy Lett. **2**, 2686 (2017).
[8] A. García-Fernández, E. J. Juarez-Perez, J. M. Bermúdez-García, A. L. Llamas-Saiz, R. Artiaga, J. J. López-Beceiro, M. A. Señarís-Rodríguez, M. Sánchez-Andújar, and S. Castro-García, J. Mater. Chem. C **7**, 10008 (2019).
[9] J. Tian, D. B. Cordes, A. M. Z. Slawin, E. Zysman-Colman, and F. D. Morrison, Inorg. Chem. **60**, 12247 (2021).
[10] T. H. Chan, N. T. Taylor, S. Sundaram, and S. P. Hepplestone, J. Phys. Chem. C **126**, 13640 (2022).
[11] G. A. Elbaz, W.-L. Ong, E. A. Doud, P. Kim, D. W. Paley, X. Roy, and J. A. Malen, Nano Lett. **17**, 5734 (2017).
[12] R. Heiderhoff, T. Haeger, N. Pourdavoud, T. Hu, M. Al-Khafaji, A. Mayer, Y. Chen, H.-C. Scheer, and T. Riedl, J. Phys. Chem. C **121**, 28306 (2017).
[13] X. Li, D. Bi, C. Yi, J.-D. Décoppet, J. Luo, S. M. Zakeeruddin, A. Hagfeldt, and M. Grätzel, Science **353**, 58 (2016).
[14] L. T. Nguyen and R. J. Cava, Chem. Rev. **121**, 2935 (2021).
[15] D. Shi, V. Adinolfi, R. Comin, M. Yuan, E. Alarousu, A. Buin, Y. Chen, S. Hoogland, A. Rothenberger, K. Katsiev, Y. Losovyj, X. Zhang, P. A. Dowben, O. F. Mohammed, E. H. Sargent, and O. M. Bakr, Science **347**, 519 (2015).
[16] O. V. Dolomanov, L. J. Bourhis, R. J. Gildea, J. A. K. Howard, and H. Puschmann, J. Appl. Crystallogr. **42**, 339 (2009).
[17] G. M. Sheldrick, Acta Crystallogr. Sect. Found. Adv. **71**, 3 (2015).
[18] G. M. Sheldrick, Acta Crystallogr. Sect. C Struct. Chem. **71**, 3 (2015).
[19] P. B. Allen, X. Du, L. Mihaly, and L. Forro, Phys Rev B **49**, 9073 (1994).
[20] G. Kieslich, S. Sun, and A. K. Cheetham, Chem. Sci. **6**, 3430 (2015).
[21] I. Spanopoulos, W. Ke, C. C. Stoumpos, E. C. Schueller, O. Y. Kontsevoi, R. Seshadri, and M. G. Kanatzidis, J. Am. Chem. Soc. **140**, 5728 (2018).
[22] P. van der Sluis and A. L. Spek, Acta Crystallogr. A **46**, 194 (1990).
[23] J. C. Hamill, J. Schwartz, and Y.-L. Loo, ACS Energy Lett. **3**, 92 (2018).
[24] D. H. Fabini, R. Seshadri, and M. G. Kanatzidis, MRS Bull. **45**, 467 (2020).
[25] O. Yaffe, Y. Guo, L. Z. Tan, D. A. Egger, T. Hull, C. C. Stoumpos, F. Zheng, T. F. Heinz, L. Kronik, M. G. Kanatzidis, J. S. Owen, A. M. Rappe, M. A. Pimenta, and L. E. Brus, Phys. Rev. Lett. **118**, 136001 (2017).
[26] T. Handa, A. Wakamiya, and Y. Kanemitsu, APL Mater. **7**, 080903 (2019).
[27] H.-H. Fang, R. Raissa, M. Abdu-Aguye, S. Adjokatse, G. R. Blake, J. Even, and M. A. Loi, Adv. Funct. Mater. **25**, 2378 (2015).
[28] N. Onoda-Yamamuro, T. Matsuo, and H. Suga, J. Phys. Chem. Solids **53**, 935 (1992).
[29] S. Govinda, B. P. Kore, M. Bokdam, P. Mahale, A. Kumar, S. Pal, B. Bhattacharyya, J. Lahnsteiner, G. Kresse, C. Franchini, A. Pandey, and D. D. Sarma, J. Phys. Chem. Lett. **8**, 4113 (2017).
[30] S. Govinda, B. P. Kore, D. Swain, A. Hossain, C. De, T. N. G. Row, and D. D. Sarma, J. Phys. Chem. **122**, 13758 (2018).
[31] A. Mohanty, D. Swain, S. Govinda, T. N. G. Row, and D. D. Sarma, ACS Energy Lett. **4**, 2045 (2019).
[32] W. Li, Z. Man, J. Zeng, L. Zheng, G. Li, and A. Kassiba, J. Phys. Chem. C 13348 (2020).
[33] D. G. Cahill, S. K. Watson, and R. O. Pohl, Phys. Rev. B **46**, 6131 (1992).
[34] A. C. Ferreira, A. Létoublon, S. Paofai, S. Raymond, C. Ecolivet, B. Rufflé, S. Cordier, C. Katan, M. I. Saidaminov, A. A. Zhumekenov, O. M. Bakr, J. Even, and P. Bourges, Phys. Rev. Lett. **121**, 085502 (2018).
[35] A. Pisoni, J. Jaćimović, O. S. Barišić, M. Spina, R. Gaál, L. Forró, and E. Horváth, J.

Phys. Chem. Lett. **5**, 2488 (2014).
[36] X. Mettan, R. Pisoni, P. Matus, A. Pisoni, J. Jaćimović, B. Náfrádi, M. Spina, D. Pavuna, L. Forró, and E. Horváth, J. Phys. Chem. C **119**, 11506 (2015).
[37] C. Ge, M. Hu, P. Wu, Q. Tan, Z. Chen, Y. Wang, J. Shi, and J. Feng, J. Phys. Chem. C **122**, 15973 (2018).
[38] A. A. Zhumekenov, M. I. Saidaminov, M. A. Haque, E. Alarousu, S. P. Sarmah, B. Murali, I. Dursun, X.-H. Miao, A. L. Abdelhady, T. Wu, O. F. Mohammed, and O. M. Bakr, ACS Energy Lett. **1**, 32 (2016).

Table 1: Fractional atomic coordinates, atom occupations and equivalent isotropic displacement parameters U_{eq} ($Å^2 \times 10^3$) at 299 K. U_{eq} is defined as 1/3 of the trace of the orthogonalized U_{IJ} tensor with uncertainty between parentheses. *(Stan: update from .cif)*

Site	**Atoms**	***x***	***y***	***z***	**occ. (%)**	**U_{eq}**
4*f*	Pb	2/3	1/3	0.3802	100	53.6 (3)
6*h*	Br	0.8314	0.1685	1/4	13 (1)	73.1 (6)
	I				87 (1)	73.1 (6)
6*g*	Br	0	1/2	1/2	40 (2)	115 (1)
	I				60 (2)	115 (1)
2*a*	MA:FA	0	0	0		
2*c*	MA:FA	1/3	2/3	1/4		

Table 2: Room-temperature dielectric constant values at several frequencies of different hybrid halide perovskites.

	ϵ_r' (300 K)				
	1 kHz	10 kHz	10^2 kHz	10^4 kHz	10^6 kHz
$MAPbI_3$	62 [28]	60 [29]	60 [28]		60 [29]
$MAPbBr_3$	60 [28]	54 [29]	50 [28]		48 [29]
$MAPbCl_3$	45 [28]		40 [28]		
$FAPbI_3$				49.4 [38]	49.4 [38]
$FAPbBr_3$				43.6 [38]	43.6 [38]
$DMAPbCl_3$		11 [8]	11 [8]		
$(FA)_{0.83}(MA)_{0.11}PbI_{2.23}Br_{0.77}$	18	18	18		

Figure Captions

Figure 1: Crystallographic structure models based on single-crystal XRD data analysis at 299 K. The gray spheres represent lead cations on 4*f* site, the violet and brown spheres represent the iodide and bromide anions on 6*g* and 6*h* sites respectively. The yellow surfaces represent the isoelectronic residual density of the organic cations on site 2*c* and 2*a*. The electron residual density represented here is ≥ 1 and ≤ 2.5 e.Å^{-3}.

Figure 2: Distortion of the dimers Pb_2X_9 in a) and along the *c* axis in b) with the bond length at 299 K. The ellipsoids represent the anisotropic thermal displacements of the atoms.

Figure 3: (a) Low magnification BF TEM images of the powder of crushed crystals, with characteristic hexagonal-shaped nanoparticles. (b) middle magnification BF TEM image of one platelet along the *c* direction. (c) [001] BF HRTEM image of the hexagonal-shaped nanocrystal and corresponding electronic diffraction (ED) pattern in the inset in the left upper corner. (d) magnified [001] HRTEM image of moiré pattern region.

Figure 4: Room temperature photoluminescent emission spectra (left axis) at different excitation wavelengths along with absorption spectra (right axis).

Figure 5: Real part of the relative dielectric constant as a function of (a) frequency at different temperatures and (b) temperature at different frequencies. The inset in (a) shows the relative dielectric loss ϵ_r'' as a function of temperature at different frequencies. The inset in (b) shows a magnified version of the figure highlighting a region of interest. For comparison, the black and purple curves were shifted upwards by adding 4 and 1 to the ϵ'_r respectively.

Figure 6: T-dependent thermal conductivity. The error bar at 320 K is indicative of the systematic uncertainty due to sample geometry that should be applied over the whole temperature range. The solid curves are the calculated minimum thermal conductivities for

related compositions (see text for more details).

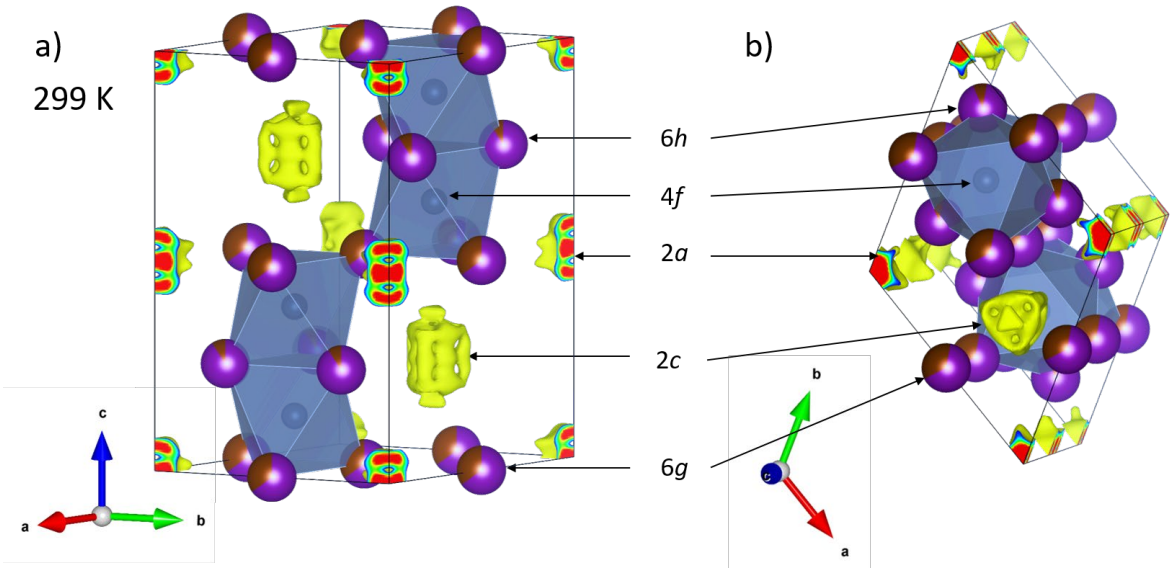

Figure 1

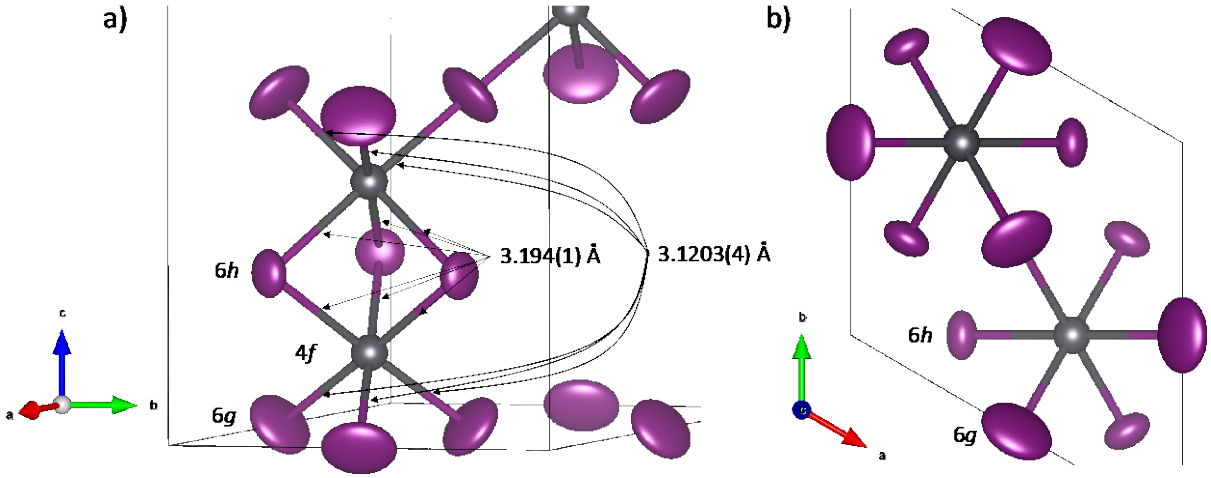

Figure 2

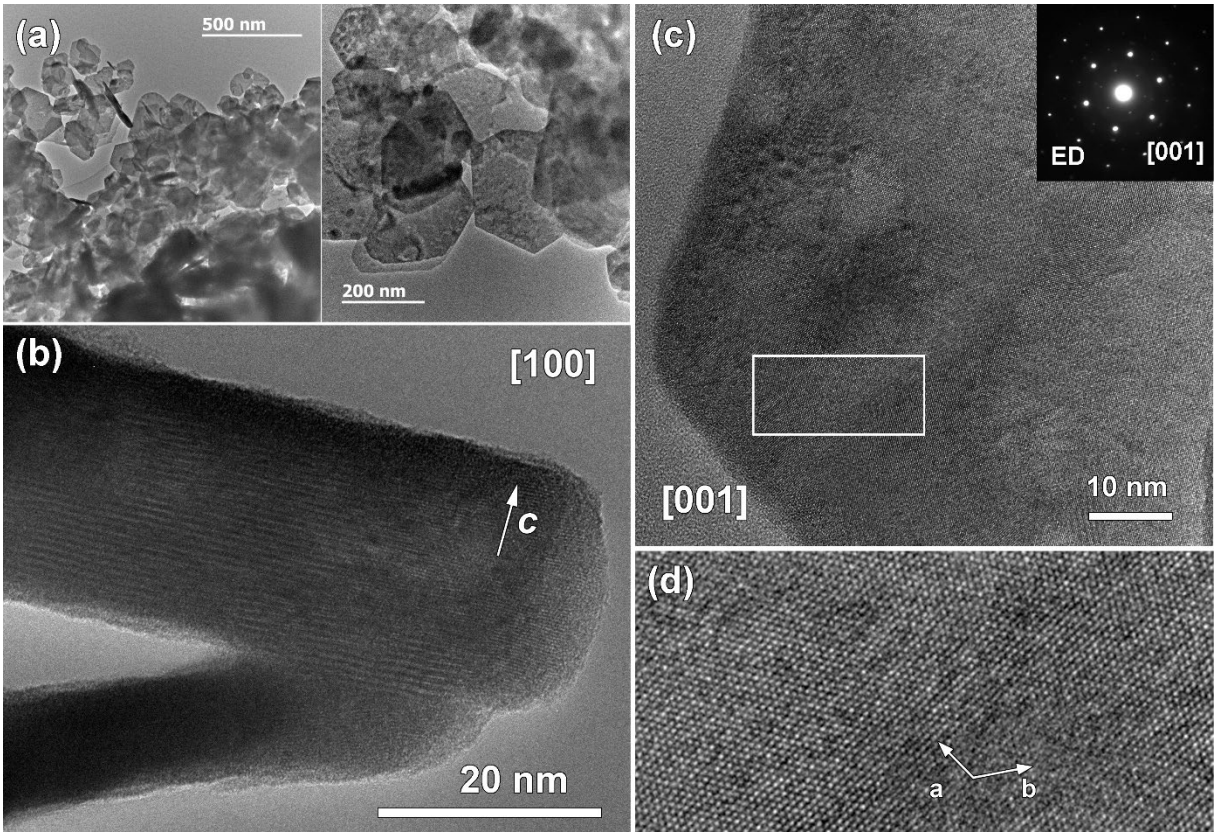

Figure 3

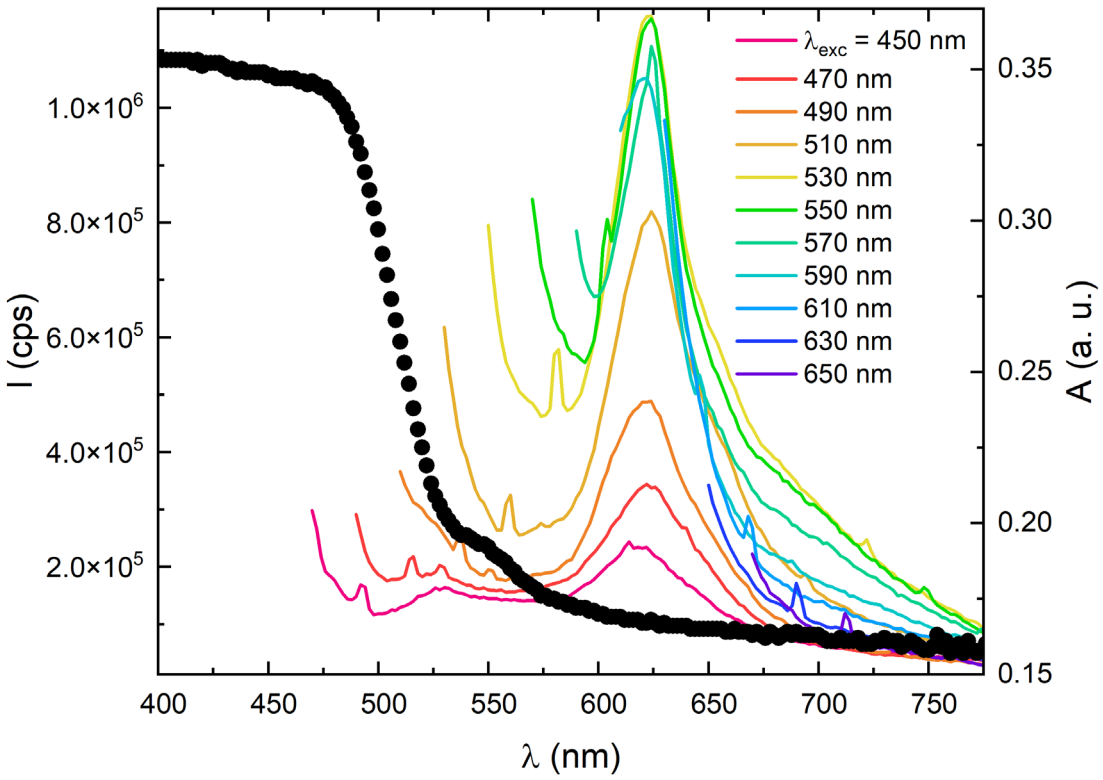
λexc = 450 nm
470 nm
490 nm
510 nm
530 nm
550 nm
570 nm
590 nm
610 nm
630 nm
650 nm
I (cps)
A (a. u.)
λ (nm)
1.0×10^6
8.0×10^5
6.0×10^5
4.0×10^5
2.0×10^5
0.35
0.30
0.25
0.20
0.15
400
450
500
550
600
650
700
750

Figure 4

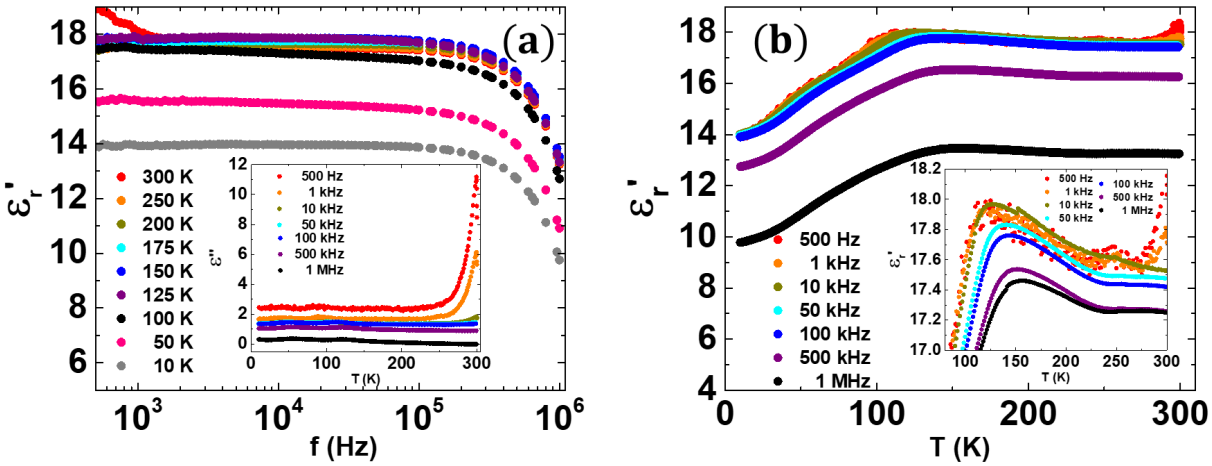
(a)
(b)
ε'r
f (Hz)
T (K)
300 K
250 K
200 K
175 K
150 K
125 K
100 K
50 K
10 K
500 Hz
1 kHz
10 kHz
50 kHz
100 kHz
500 kHz
1 MHz
ε''

Figure 5

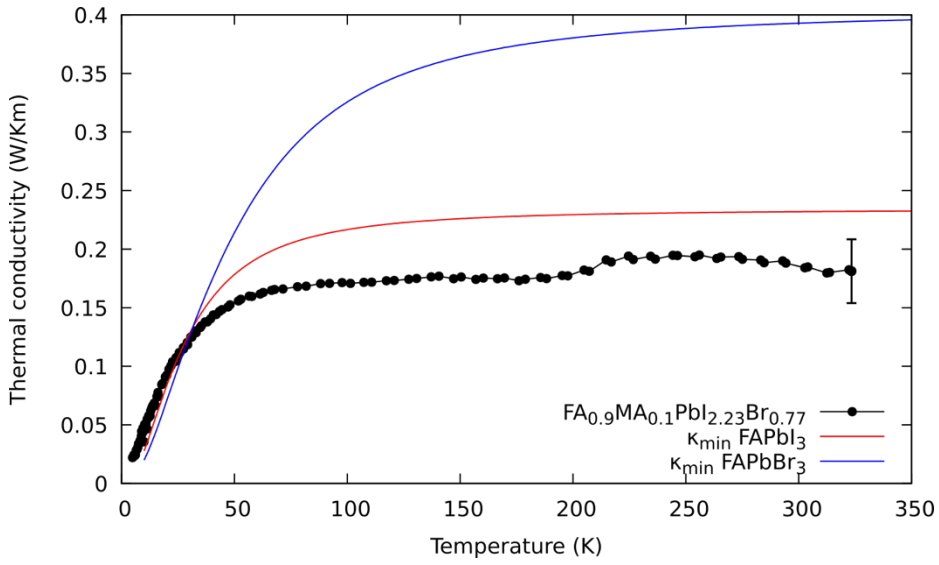
Thermal conductivity (W/Km)
Temperature (K)
0.4
0.35
0.3
0.25
0.2
0.15
0.1
0.05
0
0
50
100
150
200
250
300
350
FA0.9MA0.1PbI2.23Br0.77
κmin FAPbI3
κmin FAPbBr3

Figure 6